

## Resistive magnetohydrodynamic simulations of helicity-injected startup plasmas in National Spherical Torus eXperiment

E. B. Hooper, C. R. Sovinec, R. Raman, F. Ebrahimi, and J. E. Menard

Citation: *Phys. Plasmas* **20**, 092510 (2013); doi: 10.1063/1.4821977

View online: <http://dx.doi.org/10.1063/1.4821977>

View Table of Contents: <http://pop.aip.org/resource/1/PHPAEN/v20/i9>

Published by the AIP Publishing LLC.

### Additional information on Phys. Plasmas

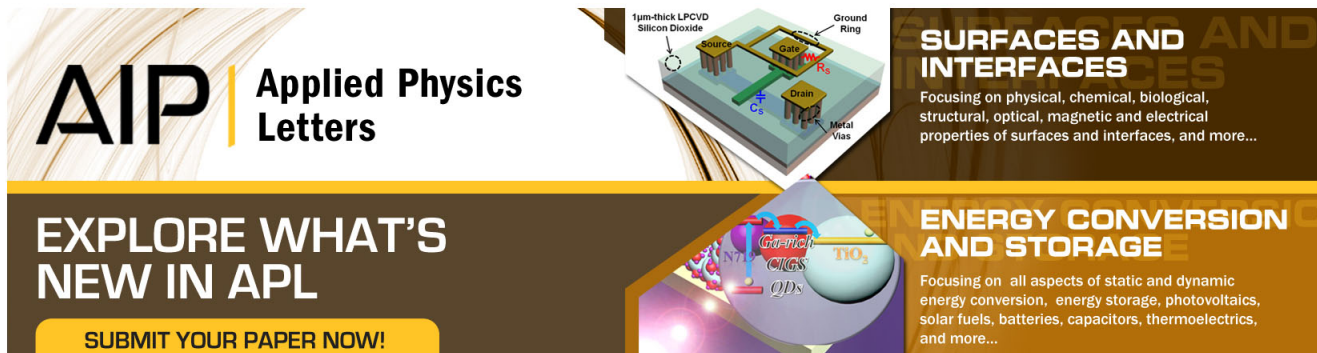
Journal Homepage: <http://pop.aip.org/>

Journal Information: [http://pop.aip.org/about/about\\_the\\_journal](http://pop.aip.org/about/about_the_journal)

Top downloads: [http://pop.aip.org/features/most\\_downloaded](http://pop.aip.org/features/most_downloaded)

Information for Authors: <http://pop.aip.org/authors>

## ADVERTISEMENT



**AIP | Applied Physics Letters**

**SURFACES AND INTERFACES**  
Focusing on physical, chemical, biological, structural, optical, magnetic and electrical properties of surfaces and interfaces, and more...

**ENERGY CONVERSION AND STORAGE**  
Focusing on all aspects of static and dynamic energy conversion, energy storage, photovoltaics, solar fuels, batteries, capacitors, thermoelectrics, and more...

**EXPLORE WHAT'S NEW IN APL**

**SUBMIT YOUR PAPER NOW!**

Labels in the 3D schematic: 1µm-thick LPCVD Silicon Dioxide, Source, Gate, Drain, Metal Vias, Ground Ring,  $C_1$ ,  $C_2$ ,  $R_1$ ,  $R_2$ .

Labels in the energy conversion diagram:  $NO_2$ ,  $CO_2$ ,  $CH_4$ ,  $QDs$ ,  $NO_3$ .

# Resistive magnetohydrodynamic simulations of helicity-injected startup plasmas in National Spherical Torus eXperiment

E. B. Hooper,<sup>1</sup> C. R. Sovinec,<sup>2</sup> R. Raman,<sup>3</sup> F. Ebrahimi,<sup>4,5</sup> and J. E. Menard<sup>5</sup>

<sup>1</sup>Lawrence Livermore National Laboratory, Livermore, California 94550, USA

<sup>2</sup>Department of Engineering Physics, University of Wisconsin, Madison, Wisconsin 53706, USA

<sup>3</sup>Department of Aeronautics and Astronautics, University of Washington, Seattle, Washington 98195, USA

<sup>4</sup>Department of Astrophysical Sciences, Princeton University, New Jersey 08544, USA

<sup>5</sup>Princeton Plasma Physics Laboratory, Princeton, New Jersey 08543, USA

(Received 30 July 2013; accepted 3 September 2013; published online 19 September 2013)

The generation of helicity-injected startup plasmas in National Spherical Torus eXperiment (NSTX), including flux surface closure, is studied using resistive-magnetohydrodynamic simulations with plasma flows, currents, ohmic heating and anisotropic thermal conduction. An injection-voltage pulse shape is used that separates the injection and closure phases allowing elucidation of the physics. The formation of an X-point near the helicity-injection gap is triggered as the injector voltage drops to zero. Near the forming X-point, magnetic pressure due to toroidal field entrained in the  $\mathbf{E} \times \mathbf{B}$  plasma flow from the helicity-injection gap drops, allowing resistive magnetic reconnection even though the total injected current is almost constant. Where appropriate, the simulations are compared with Transient Coaxial Helicity Injection experiments in the NSTX spherical tokamak, which have demonstrated the formation of a promising candidate for non-inductive startup plasmas [Raman *et al.*, Phys. Rev. Lett. **90**, 075005 (2003)]. © 2013 AIP Publishing LLC.

[<http://dx.doi.org/10.1063/1.4821977>]

## I. INTRODUCTION

The initiation of a plasma discharge in tokamaks usually utilizes a loop voltage induced by transformer action from a central solenoid, reducing the magnetic flux available for sustaining the plasma. This is a special problem in the spherical tokamak (ST), which has an aspect ratio (major radius/minor radius) close to unity, leaving minimal space for a solenoid. There is thus considerable motivation to develop alternative, non-inductive techniques to form a startup plasma with closed magnetic flux surfaces and sufficient toroidal plasma current that long-pulse or steady-state current drive can successfully build and sustain the desired equilibrium, potentially eliminating the solenoid.

We present resistive magnetohydrodynamic (MHD) simulations of magnetic field evolution and magnetic flux-surface closure in startup plasmas resulting from helicity injection in the National Spherical Torus eXperiment (NSTX). The results are compared where possible with experiments using Transient Coaxial Helicity Injection (TCHI), which have generated a startup plasma<sup>1–3</sup> followed by current build-up using ohmic drive.<sup>4–6</sup> Initially developed for use in forming and sustaining spheromaks,<sup>7</sup> Coaxial Helicity Injection (CHI) has also been applied to the ST experiments Helicity Injected Torus (HIT),<sup>8</sup> HIT-II,<sup>9,10</sup> and Helicity Injected Spherical Torus (HIST).<sup>11</sup> An electrical discharge is generated along a bias poloidal magnetic field at the plasma boundary. If the current is sufficiently large, the bias field is stretched due to  $\mathbf{J} \times \mathbf{B}$  forces, forming a poloidal “bubble,” which fills most of the available volume; for appropriate conditions, the bubble results in closed surfaces containing significant toroidal plasma current.<sup>1</sup>

For a toroidal configuration such as the ST, the application of an electrostatic voltage during CHI requires two

insulated cuts in the poloidal wall (see Fig. 1). In the ST experiments, a voltage and bias poloidal flux are applied across the lower (injector) gap. The toroidal flux injected at this gap links the poloidal flux, resulting in a helicity injection rate into the torus of twice the product of the poloidal flux across the gap and the voltage. (The factor of two arises from the definition of magnetic helicity.<sup>12</sup>) The voltage at the top gap extracts (absorbs) toroidal flux, generally at a different rate as discussed in Sec. II; from Faraday’s law, the net toroidal flux injected into the torus equals the difference in the voltage across the two gaps. This difference results in a magnetic (toroidal field) pressure across the bias poloidal flux, which, if large enough, overcomes the poloidal magnetic-field tension and expands the poloidal “bubble.” The expansion force can also be viewed as resulting from the cross-product of the injected poloidal current (driven by the injector voltage) and total toroidal field; a minimum injector current is required for the forces to be sufficiently high that the bubble “bursts” and expands.<sup>13</sup>

These simulations extend a zero-beta, resistive MHD analysis<sup>14</sup> of the HIT-II experiment using the NIMROD code<sup>15</sup> that confirmed and extended important features and scalings of CHI<sup>13,16</sup> in the high toroidal field used in tokamaks. Here, the simulation physics is expanded to include a spatially varying temperature from ohmic heating balanced by thermal conduction and the effects of the time-varying bias poloidal magnetic field used in the experiment.

The goal of this paper is to extend our understanding of the physics rather than to simulate specific TCHI discharges in NSTX. Simulations include use of applied injection voltage pulses, which differ from the experiment in order to elucidate the physics of X-point formation and flux-surface closure. Evolution of the plasma after this closure includes

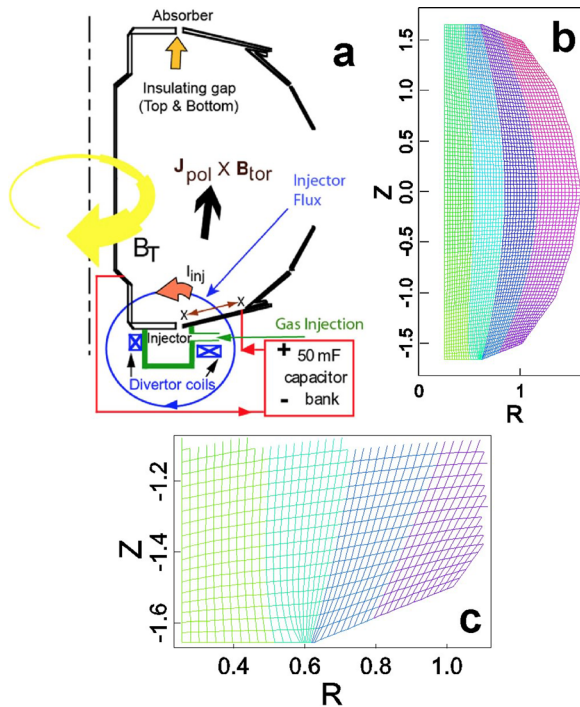


FIG. 1. (a) Schematic of the NSTX machine components including the gaps between the divertor plates, the lower divertor coils used for generating the CHI injector flux, and the absorber poloidal-field coils. The injector gap width in the simulations (4 cm) is the same as the experiment. In these simulations, the central column boundary had a constant radius equal to the experimental value at top and bottom, and the absorber PF coils were not energized. (b) The computational grid used in the simulations. (c) Expansion of the grid showing the packing above the injection gap.

effects of the experimental bias poloidal-field evolution. Magnetic flux-surfaces are found to close in the axisymmetric approximation due to resistivity, with no symmetry-breaking magnetic fluctuations required. The trigger for closure is the reduction in toroidal magnetic pressure near a forming X-point as the applied voltage is dropped. Further, detailed analysis of the plasma flows and currents during closure are examined elsewhere using a simpler, zero-beta model of the plasma.<sup>17</sup>

Experiments have several differences from these simulations. The measured electron temperatures during CHI-only discharges (i.e., with no inductive drive) are lower than in these simulations, and closed-flux volumes are greater in the experiment. In the experiments, the injector current drops more rapidly than in the simulations as the voltage is dropped following injection, apparently due in part to these lower temperatures and in part to a series resistor in the power supply. Also, as discussed in Sec. II, the absorber poloidal-field coil currents are set to zero in the simulations. Understanding the consequences of these and other differences between the simulations and the experiment is the subject of ongoing research.

Section II compares the simulation and experimental geometries and discusses the boundary conditions. Section III provides an overview of the simulated discharges and describes the injection phase. Section IV focuses on the evolution in the simulations following helicity injection, including the flux-surface closure event and subsequent plasma evolution, and Sec. V gives conclusions.

## II. SIMULATION GEOMETRY, BOUNDARY CONDITIONS, AND PLASMA PARAMETERS

A schematic of the NSTX is shown in Fig. 1. The boundary in the simulation<sup>18</sup> is similar to the experiment; it surrounds the poloidal cross section and is perfectly conducting from the perspective of the plasma except in the insulating gaps. The poloidal magnetic field normal to the boundary can be determined in two ways: from the external poloidal-field coils alone or from a time-dependent, boundary-condition calculation that includes the coils and eddy currents in the NSTX structure. The latter is generated using the applied (vacuum) fields from an experimental discharge (142163 in this paper) and is used unless indicated otherwise. The vacuum toroidal field is generated by a constant current along the geometric axis.

The gap boundary conditions<sup>18</sup> generalize those in the HIT-II simulations.<sup>14</sup> A voltage,  $V_{inj}$ , is applied across the injector gap; the results presented here use a model of the NSTX capacitor-bank power supply. The injector current,  $I_{inj}$ , is determined by the plasma impedance load on the power supply. It is measured by the change in toroidal magnetic field above the gap and feeds back to evolve the charges and voltages in the capacitor bank. The vacuum toroidal flux carried in by plasma  $\mathbf{E} \times \mathbf{B}$  flow at the injector is extracted by the flow at the absorber on the top of the machine, resulting in constant vacuum toroidal flux in the vessel. This is consistent with the experiment; the change in toroidal flux measured by diamagnetic loops and the change in the simulations are similar in magnitude and small,  $\ll 1\%$  of the vacuum flux. Net flux injection results from the increase at the injector of the toroidal field above the vacuum value; as this increase is much less than the vacuum field, the voltages across the gaps differ only slightly in the simulations. Following the injection phase, the currents decay and the sign of the difference reverses as toroidal flux is lost.

The required outward flow at the absorber gap is at the local  $\mathbf{E} \times \mathbf{B}$  velocity. In the simulations, this generates currents that are absent or small in the experiment as there is little or no plasma there. These currents have only a local effect (including heating), but to minimize them the absorber coils are not energized in these simulations and a low-temperature layer is inserted in the top 5 computational cells. In addition, a narrow, high resistivity boundary layer is placed along the top and bottom plates to allow currents to diffuse along them until reaching force-balance.

The calculations used Spitzer resistivity and a kinematic viscosity of  $50 \text{ m}^2/\text{s}$  to ensure numerical stability; this is on the low end of the value ensuring stability, and previous studies had shown only small quantitative changes with the value. Thermal diffusivity along the magnetic field equals the Spitzer-Braginskii electron parallel value ( $387 T^{5/2} \text{ m}^2/\text{s}$ ), and the cross-field diffusivity is spatially constant in each simulation as no experimental estimates are available. Typically,  $0.5$  to  $3 \text{ m}^2/\text{s}$  is used, with the precise value resulting in only quantitative effects, e.g., broadening the temperature peak where the injected current flows in the plasma. Density is held approximately constant by a large diffusion coefficient in the continuity equation, which is expected to

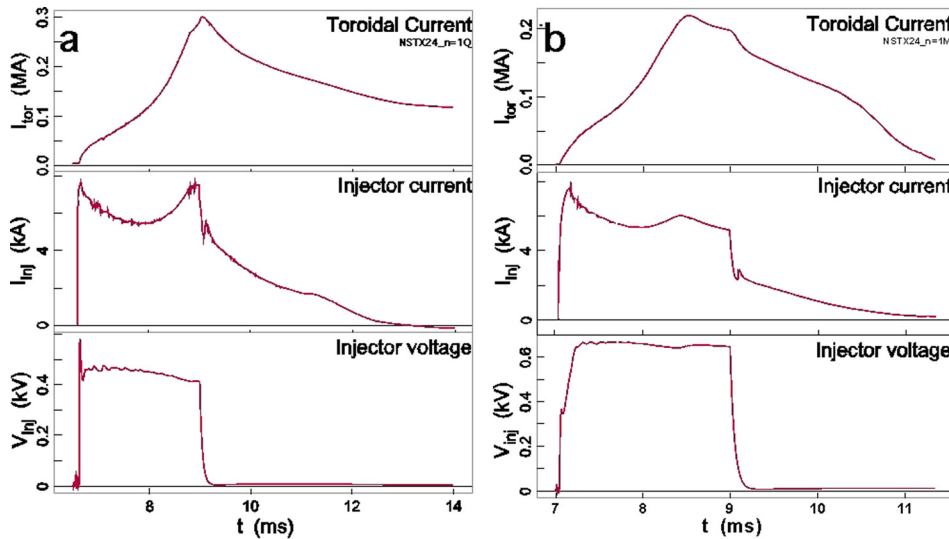


FIG. 2. Discharge characteristics for (a) *hi-temp* and (b) *low-temp*. Bottom to top: Injection gap voltage, injection current and toroidal current for simulation *hi-temp*, which includes the toroidal  $n=0$  and 1 modes. The power supply used a large capacitor to give a nearly flat voltage pulse and the currents are measured. Note the different time scales.

have minor effects, primarily on energy conservation if compressibility is low<sup>19</sup> as found in CHI simulations of a spheromak.<sup>20</sup> A  $45 \times 90$  poloidal grid (Fig. 1) with radial packing above the injector gap was used. Lagrange elements of order 4 in the grid cells<sup>15</sup> gave converged simulations, as found in studies varying the order from 2 to 5.

### III. SIMULATIONS OF HIGH AND LOW TEMPERATURE CHI DISCHARGES

Currents and injection voltage for two simulated discharges are shown in Fig. 2. The simulation in Fig. 2(a) (*nIQ*; hereafter *hi-temp* to characterize its features) was chosen because it is a high-quality discharge in the sense that the toroidal current remains high to the end of the simulation at 14 ms. As will be seen below, by 14 ms, the toroidal current flows fully within the closed flux surfaces. This simulation had no impurities or radiated power, which together with a low perpendicular thermal diffusion coefficient yielded electron temperatures of about 140 eV at  $z=0$  with a peak of 160 eV at higher  $z$ , greater than in the experiment where the measured electron temperatures during in CHI-only discharges (i.e., with no inductive drive from the transformer) are in the 20–30 eV range at  $z=0$ .<sup>1</sup>

Figure 2(b) (*nIM*, hereafter *low-temp*) includes a generic radiation model that increases monotonically with temperature resulting in the temperature in the current layer dropping to a peak value of 50 eV and to  $\sim 3$  eV in the core plasma. The peak temperature is still higher than measured in the experiment, but the result suggests that impurity radiation may be important for detailed comparisons with experiment. Both the injector and toroidal currents drop more rapidly than in *hi-temp*, reaching zero soon after 11 ms. The temperature profiles are compared in Fig. 3; the high-temperature peaks form in the channel at the surface of the expanded flux (Fig. 4) where most of the injector current flows.

In both simulations, an X-point forms above the injector gap  $< 100 \mu\text{s}$  after 9 ms when the applied voltage is dropped. The “jogs” seen in the injector currents for both simulations occur when the X-point forms. The *low-temp* simulation will

be used in the next section to identify the mechanism that triggers this event.

The injection voltage is dropped more rapidly than in the experiment to transition quickly (but smoothly) to the non-injection state. In the simulation, the power supply is effectively short-circuited after the extractor voltage reaches zero, ensuring no voltage across the extractor gap. However, the rate of injector current drop is much slower than in the experiment, especially in *hi-temp*. This is due (at least in part) to the higher temperature therein as can be seen by comparing the injector-current decay rates in Fig. 2.

Selected poloidal flux surfaces from *hi-temp* are shown in Fig. 4 along with photographs of visible light from an experimental discharge. Although these simulations did not have injection parameters identical to those of the experimental discharge, the plasma developed in a very similar way. In experiments, large-volume, closed flux surfaces were found in magnetic reconstructions<sup>1</sup> soon after voltage and current reduction. (As the Alfvén time is much shorter than other plasma times, the plasma is in an approximate Grad-Shafranov equilibrium, albeit with currents on open field lines until the injector current is reduced to zero.) The radii of the largest surfaces in the experiment (1.5 m at the

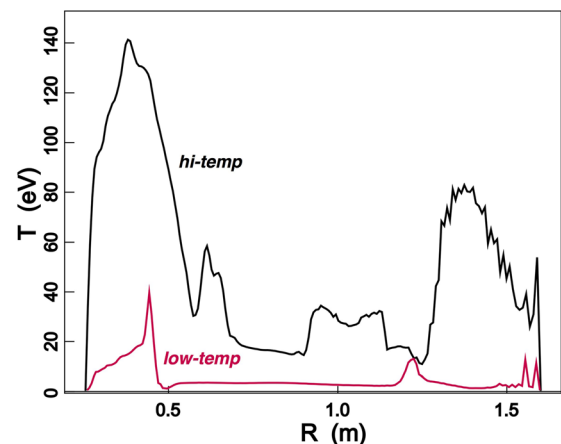


FIG. 3. Temperature profiles at the midplane ( $Z=0$ ) for the *hi-temp* and *low-temp* simulations at 9 ms.

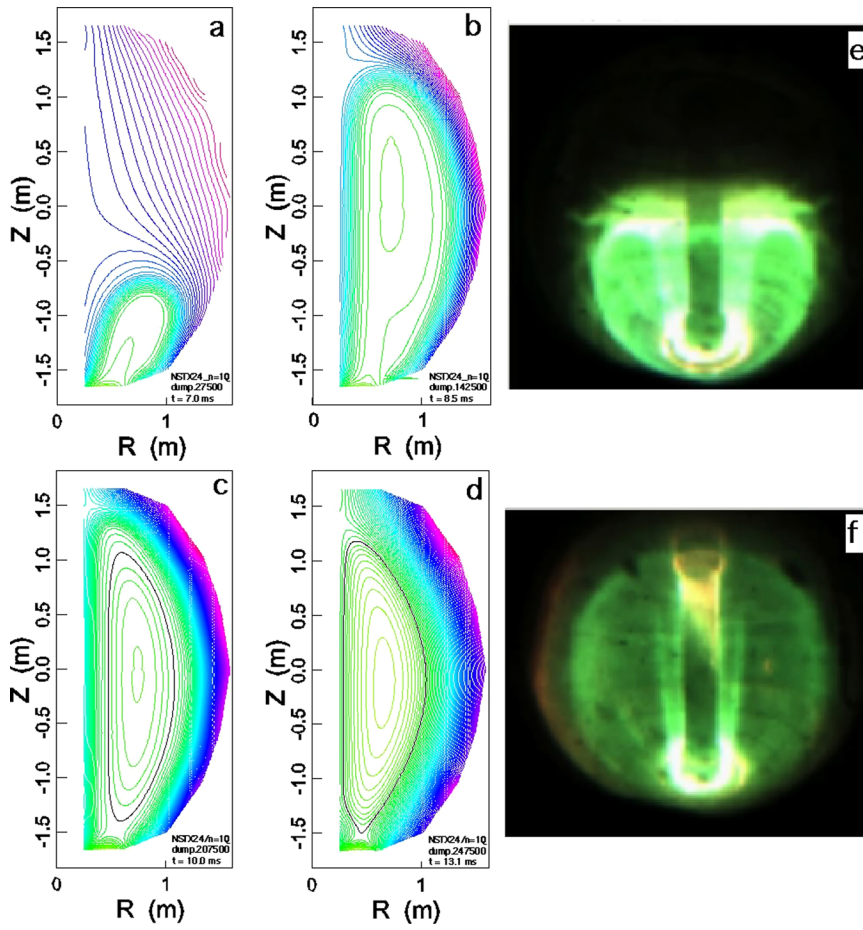


FIG. 4. Time-dependent poloidal-flux surfaces of the injected plasma: simulation *hi-temp* at (a) 7.0 ms, (b) 8.5 ms, (c) 10.0 ms, and (d) 13.1 ms. The poloidal surfaces in (a) and (b) are spaced at 2.1 mWb, in (c) and (d) at 1.1 mWb. Photographs of experimental discharge 142163: (e) 7.0 ms and (f) 8.4 ms.

midplane vs. 1.3 m in simulations) extend closer to the outer boundary (1.6 m) of NSTX with a smaller volume of external open flux than in *hi-temp*. Improving agreement with the experimental results is the subject of on-going studies.

In the simulation, the toroidal current is strongly peaked near the separatrix, resulting in an internal inductance of about 0.2. The safety factor is large, even in the interior of the plasma; for example, at 10 ms (Fig. 4), it is  $\approx 50$  at the magnetic axis due to the low plasma currents there. The current multiplication is also large, e.g.,  $I_{tor}/I_{inj} \approx 40$  at 9 ms.

#### IV. X-POINT FORMATION AND FLUX CLOSURE

The poloidal-flux contours at the end of injection (9 ms) for the two simulations are plotted in Fig. 5. Although *low-temp* had a shorter injection time than *hi-temp*, the applied voltage was higher, resulting in nearly identical toroidal flux injections ( $\approx 1.3$  Wb) and similar expansions of the bias poloidal flux. The injected current flows primarily in the large-gradient layer of stretched poloidal flux, although the low temperature in *low-temp* causes more magnetic diffusion than in *hi-temp*.

X-points form above the injector slot in both simulations. Symmetry-breaking, MHD oscillations play no role. Both simulated plasmas are nearly axisymmetric and do not exhibit the global, toroidal  $n=1$  mode observed in spheromaks<sup>21</sup> and strongly driven STs.<sup>9</sup> In these simulations, a ribbon-like  $n=1$  mode often observed in the current layer on the flux-bubble surface during injection simulations<sup>22</sup> has

little effect on flux-surface closure, confirmed by comparing axisymmetric simulations with ones including the mode. In addition, flux-surface closure is observed in fully axisymmetric simulations.<sup>5,6,17</sup>

Let us consider the X-point formation in the *hi-temp* simulation first. As seen in Fig. 4, closed flux surfaces start forming near the midplane during injection at about 7.5 ms

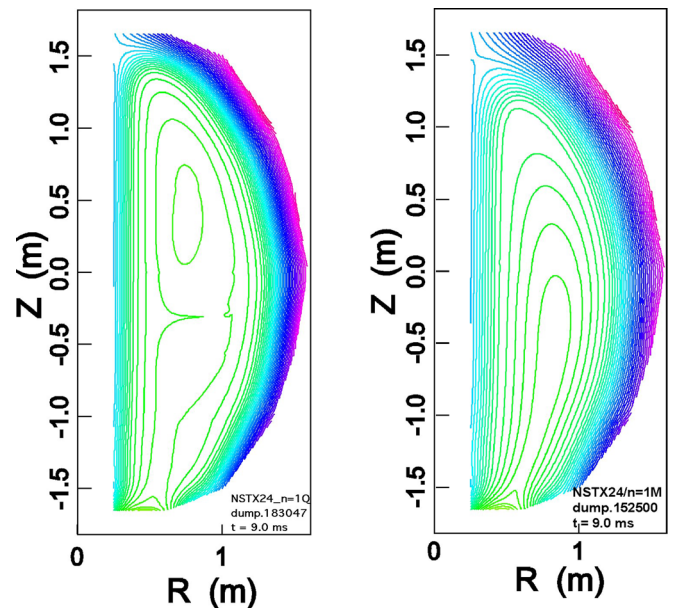


FIG. 5. Poloidal flux at 9.0 ms (a) *hi-temp* and (b) *low-temp*.

when a region of nearly constant poloidal flux forms; the amount of closed poloidal flux is  $\sim 0.1$  mWb, much less than the total flux in the bubble,  $\sim 30$  mWb. This region grows in time and a second, shallow region forms below it at about 9 ms, but no large-volume, closed surface forms during injection. (The second region is not resolved in Fig. 5.) Both the toroidal current (11 kA at 9 ms) and toroidal flux enclosed in the surfaces remain small as long as the injection voltage is applied and are inadequate for a startup plasma. However, when the voltage across the injection gap drops close to zero, a clearly defined closure event occurs at about 9.1 ms. The resulting closed volume in *hi-temp* has a X-point near the bottom of NSTX and a separatrix outside the closed volumes formed during injection.

The structure of the shallow closed-flux regions at 9 ms in *hi-temp* complicates the interpretation of the mechanism triggering the formation of the X-point near the bottom of NSTX. However, in *low-temp*, there are no pre-existing closed surfaces at 9 ms, and the closure-event still is triggered by the applied voltage drop.

Field-line (“Poincaré”) puncture plots in *low-temp* just before and near the end of closure are shown in Figs. 6(a) and 6(b). The injection voltage and  $\mathbf{E} \times \mathbf{B}$  flow from the gap has dropped to near zero at the closure time, greatly reducing the plasma flow through the narrow neck as seen in Figs.

6(c) and 6(d). As quantified below, toroidal magnetic flux is entrained in the flow, resulting in an axisymmetric magnetic pressure, which drops as the injection voltage and flow drop. When the flow drops sufficiently, the magnetic fields on the sides of the channel reconnect resistively, triggering flux closure.

The temperature in the neck region is about 15 eV in a region 2.5 cm wide and less outside that region. The magnetic diffusion time is  $\sim \Delta x^2 / D_m$ , with  $D_m \approx 411 T_e^{-3/2} = 7$  m<sup>2</sup>/s, so reconnection will occur in  $< 100 \mu\text{s}$ , in agreement with this simulation. (See Ref. 17 for a comparison of the resistive scaling with the Sweet-Parker model.) Dissipation during the closure increases the temperature inside the resulting closed flux volume by 5–10 eV.

It remains to quantify the magnetic pressure effect. A radial plot of magnetic fields and pressure from the simulation in the vicinity of the “finger” of flux (Fig. 6) are shown in Figs. 7 and 8. During slowly varying equilibria, magnetic forces are approximately in equilibrium due to the low beta and flow velocities. The poloidal component of pressure balance can be written as

$$\nabla_p \frac{B^2}{2} - \left[ \mathbf{B}_p \cdot \nabla \mathbf{B}_p - \frac{B_\phi^2}{r} \hat{\mathbf{r}} \right] = 0, \quad (1)$$

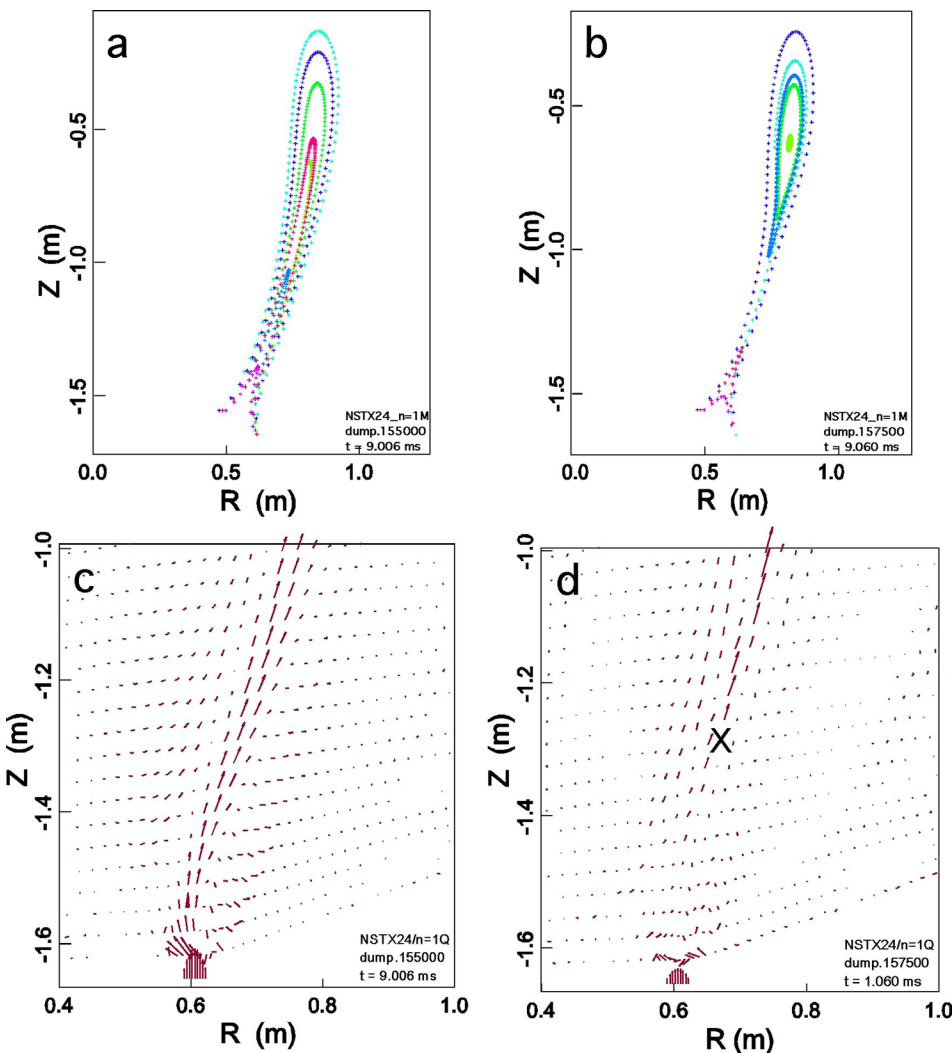


FIG. 6. Poincaré puncture plots (a) before (9.006 ms) and (b) near the end (9.060 ms) of the closure event in *low-temp*. (c) and (d) Poloidal flow velocity vectors corresponding to (a) and (b). The vectors are plotted at the same scale. The X-point (marked in (d)) forms at  $R = 0.6750$  m,  $Z = -1.2838$  m. The flow through the gap (at  $R = 0.6$  m) is proportional to the injection voltage, which has dropped at 9.06 ms to 195 V, 30% of the 9.0 ms value.

where the subscript  $p$  indicates the poloidal component.

To interpret the fields and pressure, consider an approximate solution to the radial component of Eq. (1). In the vicinity of the finger where the poloidal field has a zero (see Fig. 7), the poloidal field lines are nearly straight ( $\mathbf{B}_p \cdot \nabla B_r \approx 0$ ) so that the poloidal contribution to the curvature can be neglected relative to the toroidal contribution. Next, separate  $B_\phi$  into the vacuum ( $B_{\phi 0} \approx 1$  T) and driven ( $\delta B_\phi$ ) parts and expand  $B_\phi^2$  in Eq. (1). It is noted that because  $rB_{\phi 0}$  is constant the terms in  $B_{\phi 0}^2$  cancel and do not contribute to the net force balance. The radial component of Eq. (1) becomes

$$\frac{\partial}{\partial r}(2B_{\phi 0}\delta B_\phi + \delta B_\phi^2 + B_R^2 + B_Z^2) \approx -2\frac{2B_{\phi 0}\delta B_\phi + \delta B_\phi^2}{r}. \quad (2)$$

Integrating Eq. (2) with respect to  $r$  yields twice the magnetic pressure,  $\delta W$

$$\begin{aligned} \delta W &\equiv 2B_{\phi 0}\delta B_\phi + \delta B_\phi^2 + B_R^2 + B_Z^2 \\ &\approx -4 \int \frac{B_{\phi 0}\delta B_\phi + \delta B_\phi^2/2}{r} dr + const. \end{aligned} \quad (3)$$

It needs to be emphasized that this approximation breaks down where the poloidal curvature is not small. However, in the present case with small curvature, the poloidal field is almost vertical, which further reduces the contribution from residual poloidal curvature: from Fig. 7, the jump (across the flux finger, from right to left in Figs. 7(c) and 7(d)) in  $B_R^2 \approx 0.16$  times the jump in  $B_Z^2$ , so any poloidal-curvature contribution is reduced by a similar magnitude.

Fig. 7(a) shows a radial cut of  $\delta B_\phi$  slightly below the X-point forming in Fig. 6. There are two parts to  $\delta B_\phi$ : a slowly varying, first part due to the bulk of the injector current and a second part due to the fields generated by currents

near and in the finger. As most of the injected current flows near the surface of the injected flux-bubble the first part drops very nearly as  $1/r$  inside the surface. Neglecting the contribution from  $\delta B_\phi^2$  the contribution to the integral in Eq. (3) thus is approximately  $2(rB_{\phi 0})(r\delta B_\phi)/r^2$ . This is the slowly dropping field in Fig. 7(a). The contribution to the integral from the currents forming the finger is the product of two small terms,  $\Delta(\delta B_\phi) \ll \delta B_\phi$  and  $\Delta r \ll r$ , and is small. We thus anticipate that when the magnetic configuration is in a near-equilibrium state, the magnetic pressure is nearly constant in the finger region except for the slowly varying term  $\approx 2(rB_{\phi 0})(r\delta B_\phi)/r^2$ .

The fields at  $t = 9.006$  ms (just before the X-point formation event) are shown in the region of interest in Figs. 7(b)–7(d). The null points in the radial and vertical fields show where the poloidal field passes through zero in the center of the flux finger; the toroidal field has a local maximum in the finger where toroidal flux is carried by the flow from the injector slot. Magnetic pressures are presented in Fig. 8(a) just before the reconnection (9.006 ms), and as in Eq. (3) drops smoothly through the poloidal-field null before the X-point forms. During the reconnection (9.060 ms, Fig. 8(b)) the perturbed pressure due to the toroidal field drops when the flow from the slot drops (Fig. 6) and no longer cancels out the poloidal-field variations. The field is not in pressure equilibrium ( $\mathbf{j} \times \mathbf{B} \neq 0$ ); magnetic pressure adjacent to the poloidal-field null exceeds pressure at the null, and the associated Lorentz force density drives flow and field-lines into the null from both sides. By 9.216 ms, the X-point has formed. Fields vary smoothly with radius and the curvature is not negligible due to the nearby X-point.

The plasma is axisymmetric so the closure occurs from resistive effects and can be characterized as a Sweet-Parker reconnection process. Details of the reconnection including

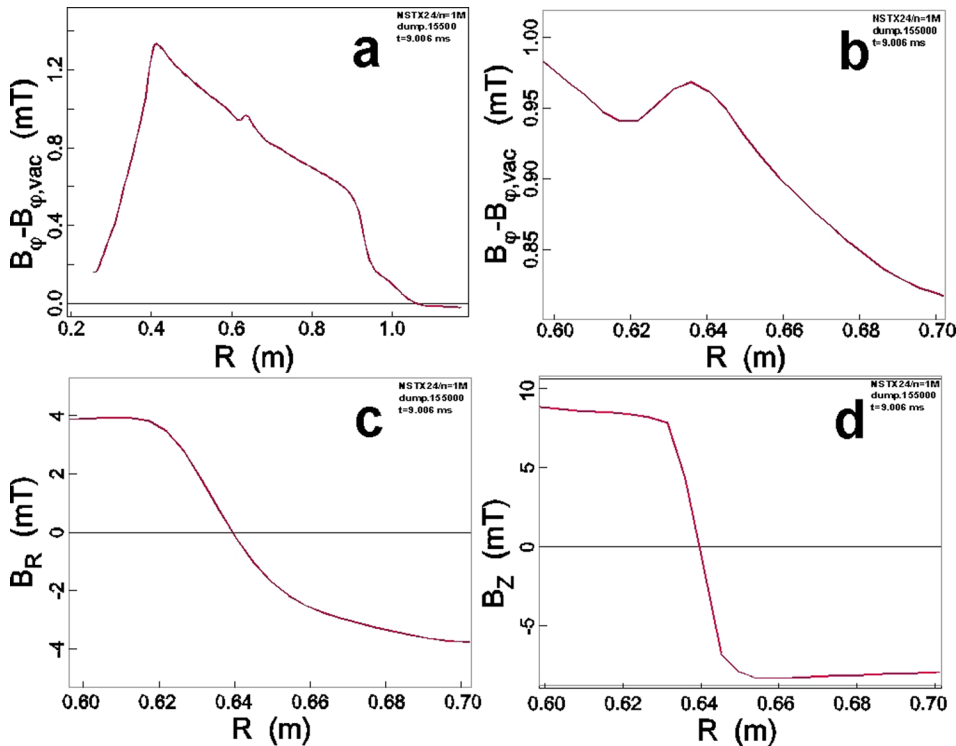


FIG. 7. Fields and energy at 9.006 ms and  $z \approx -1.34$  m. (a) and (b)  $\delta B_\phi$  vs.  $R$ , (c)  $B_r$ , and (d)  $B_z$ ; (b)–(d) span the finger shown in Fig. 6. The small “bump” in (a) and expanded in (b) is due to the toroidal field carried by flow into the finger.

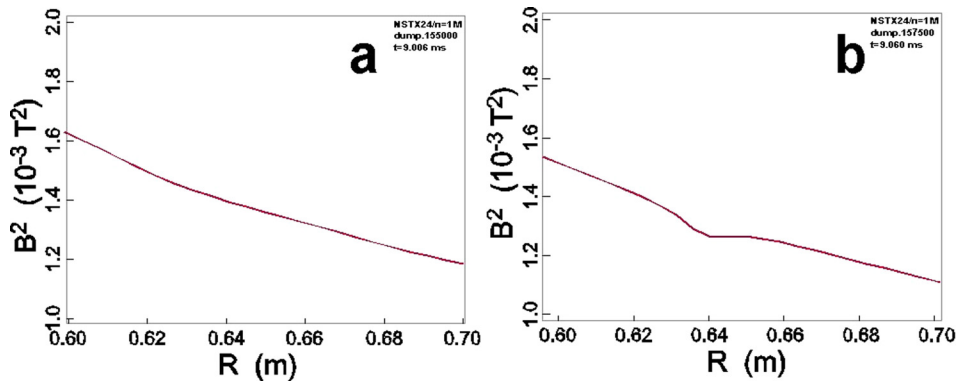


FIG. 8.  $\delta W$  at (a)  $t = 9.006$  ms, (b)  $t = 9.060$  ms;  $z = -1.34$  m. The negative 0.05 mT bump of toroidal field evident in Fig. 8(b) results from the reduction in  $\delta B_\phi$  as discussed in the text.

plasma flows and currents are presented elsewhere.<sup>17</sup> An elongated current sheet is shown to form along the flux-finger (Fig. 6) with a width that scales as the square-root of the magnetic diffusivity. The cross-field plasma flow into the current sheet at the poloidal-field null is due to the pressure imbalance when the injector voltage drops and occurs at the local  $\mathbf{E} \times \mathbf{B}$  (nearly radial) velocity.

In the simulations, the closure event is thus triggered by the drop in the local magnetic pressure when the flow from the injector falls, allowing the X-point to form. In *low-temp*, the closed volume grows for a short time ( $\sim 60 \mu\text{s}$ ) but then decays to the end of the simulation (11.3 ms) due to the low temperature. In *hi-temp*, the larger volume (Fig. 4(c)) occurs when the resulting separatrix surrounds the closed regions formed during injection. It lasts beyond the end of the simulation at 14 ms.

An additional simulation in Fig. 9 demonstrates that the event is not triggered by the rate at which the injector voltage drops. The voltage dropped significantly but slowly during injection and the X-point formed at 8.5 ms before the voltage was decreased to zero at 9.0 ms. The injector current is also nearly constant at the time of closure; the closure is associated with changes in currents associated with the flow near the narrow flux region (as in Fig. 6). At the time of closure, the voltage was about 130 V, similar to the *hi-temp* and *low-temp* values.

Finally, simulations show that flux-surface closure is not due to the time-varying boundary conditions or the ohmic heating. In simulations with constant boundary poloidal flux and no ohmic heating or temperature-dependent resistivity, a closed volume of flux surfaces is triggered by the same mechanism as above.<sup>17</sup>

## V. EVOLUTION FOLLOWING FLUX-SURFACE CLOSURE

The plasma evolution following the flux closure event is examined using the *hi-temp* simulation with its relatively large volume of flux surfaces. In Figure 10, the total toroidal current is plotted along with the current inside the closed volume. The latter is small ( $\approx 20$  kA) immediately following closure but grows until equaling the total current, after which it decays resistively. Also shown is the evolution of closed current when the surface poloidal flux is held constant following the closure event. Note, however, that the flux-closure event still occurs when the surface flux is held constant.<sup>17</sup>

Following formation of the X-point in *hi-temp*, the enclosed toroidal plasma current approaches the total current at about 13.2 ms. This is the time at which the injector current,  $I_{inj}$ , reaches zero, as can be seen in Fig. 2(a). Although it is considerably later than in the experiment (11.6 ms), it is in agreement with the experimental conclusion that  $I_{inj} = 0$  with  $I_{tor} \neq 0$  demonstrates that the measured toroidal current flows in closed surfaces.<sup>1</sup>

Because the surfaces are closed and the voltage across the injector gap is zero, the increase in confined current when the surface poloidal flux changes but not when it is held constant shows the effect of a loop voltage induced by the changing poloidal flux on the boundary. In the experiment, a loop voltage measurement below and slightly outside the injector gap shows  $\sim 12$  V due to the time-changing injector coils; this and associated eddy currents are included in the time-dependent, poloidal-flux boundary conditions on the computational domain. Although the eddy currents reduce the inductive voltage, examination of the rate of flux change on the boundary shows that the induced voltage in the hole of the toroidally closed surfaces during this time is

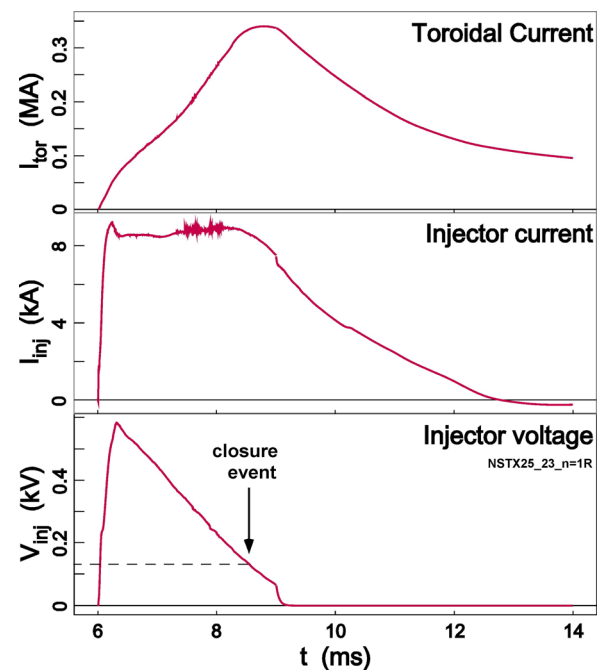


FIG. 9. A simulation with closure before the injection voltage is decreased to zero.

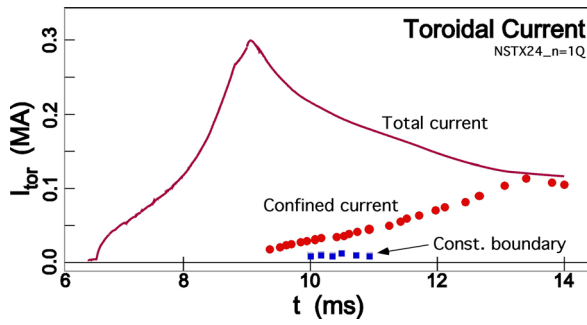


FIG. 10. Evolution of toroidal plasma current following flux-surface closure in *hi-temp*. The red circles show the current within the closed flux, and the blue squares show the enclosed toroidal current when the boundary poloidal flux is constant after the X-point formation.

sufficient to drive the change in current in the closed flux region.

Analysis of the toroidal flux within the closed flux reaches a similar conclusion to that for enclosed toroidal current. Figure 11 shows the net toroidal flux in the simulation. During the CHI phase of the experiment, the two gap voltages differ only by the small amount needed to generate the excess magnetic pressure within the flux bubble and the corresponding injected current. The net flux change, shown in Fig. 10, is much less than the vacuum flux ( $\approx 2.53$  Wb). This toroidal flux,  $\approx 4.0$  mWb, is in approximate agreement with the change measured in the experiment when the flux-bubble nearly fills the volume.

The net toroidal flux confined in the closed flux surfaces equals the total net flux when the injector current reaches zero. As seen in Figs. 2 and 9, this current, driven by the plasma inductance, drops to zero in 2–4 ms in these simulations; the decay rate is determined by the plasma resistivity and any resistance across the injector gap (zero in the simulations presented here). Note that injector currents also flow in the private-flux region below the X-point.

## VI. DISCUSSION AND CONCLUSIONS

The simulations presented here demonstrate the buildup of a plasma in the NSTX geometry by injection of toroidal

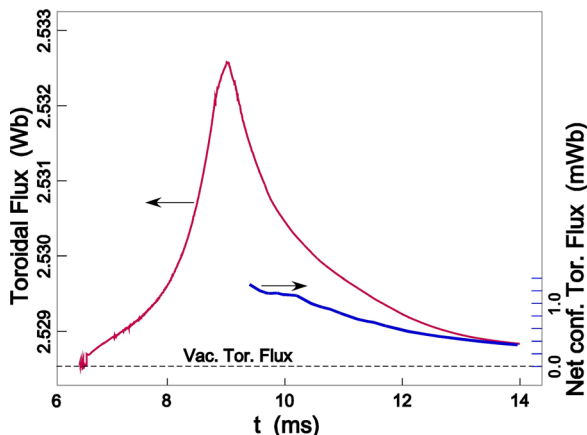


FIG. 11. Toroidal flux. Shown are the total toroidal flux change within the computational boundary for the *hi-temp* simulation and the net toroidal flux (flux—vacuum flux) within the closed surfaces following the flux-closure event.

flux and helicity, identify the mechanism forming the X-point above the injector slot following the end of injection, and follow the subsequent evolution of the plasma. The model includes ohmic heating and thermal conduction and the time-varying, vacuum poloidal-field used in the experiment. Unless impurity radiation is included, the temperature in the simulations is considerably higher than measured in experimental discharges. Future work will further explore the role of impurities to determine the effects on closure and the subsequent evolution of the plasma, allowing detailed comparison with experiment. Initial simulations, however, show the same X-point formation mechanism as described here.

Most of the simulations presented here used injection pulses that were nearly square, providing a separation between the injection and flux-closure phases of CHI in a resistive MHD model of NSTX. This allowed the determination that the closure event following the end of injection is due to changes in the magnetic pressure when the plasma flow from the injector drops in the vicinity of the forming X-point.

In the present *hi-temp* simulation, a large volume of closed flux forms in a series of steps. First, areas of closed flux form resistively inside the layer of injected current during helicity injection. This occurs where the poloidal flux is nearly flat, and the resulting toroidal current inside the closed surfaces is small. It is unclear whether a similar effect occurs in the experiment. Then, when the applied voltage and associated plasma flow is dropped to zero after injection, an X-point forms resistively; the resulting separatrix surrounds the areas of closed flux. The enclosed toroidal current and flux then grow due to the inductive effects of the changing poloidal flux on the conducting, computational boundary (due to external magnetic coils). High temperature provides a relatively low-resistance path for the current, and following injection, the decay of plasma current is slow enough that the external induction can significantly increase the enclosed current and flux. The use of the NSTX transformer to further increase the current has not been simulated.

The value of the peak electron temperature in the *low-temp* simulation is  $\sim 50$  eV. The resulting poloidal-flux contours vary throughout the interior of the flux “bubble.” No closed surfaces form during injection, presumably because of this variation.

While the simulation *hi-temp* agrees with the experiment at 13.5 ms, there are other major differences with the experiment that this simulation does not capture the following:

- (1) The biggest difference is that in the experiment, the injector current goes to zero at 11.5 ms. At this time, there is 154 kA of closed flux current that decays to 106 kA at 13.6 ms. The simulated injector current goes to zero at 13.6 ms. In the simulations, at 11.5 ms, there is only 50 kA of closed flux current. This increases to 118 kA at 13.5 ms. So, experimentally, the closed flux current decays in time, at a rate consistent with a low temperature plasma, whereas the simulated closed flux current increases in time.
- (2) If the peak  $T_e$  is reduced to 50 eV as in *low-temp*, which is still much higher than the experimental value, then

only small, short-lived closed flux surfaces form in the simulation.

- (3) In calculating the boundary flux, the currents in the upper absorber coils are ignored in the simulation.
- (4) Finally, the initial evolution of the discharge is quite different. Experimentally, the toroidal current grows to 330 kA at 8.43 ms. The current reaches full value in 2 ms ( $dI/dt \sim 165$  kA/ms). In the simulations, the growth rate is slower, and it has a different shape and gets to 303 kA at 9.04 ms—in 2.64 ms ( $dI/dt \sim 115$  kA/ms).

Addressing these important differences is necessary for using NIMROD results in a predictive mode.

As part of this effort, studies are on-going to benchmark fully the model against experimental results. The demonstration of large-volume flux surfaces, although of smaller volume than in the experiment, will be extended to include the sensitivity to parameters such as time-dependent injection voltage and current, the power-supply impedance across the gap following injection (which will affect the final closed flux and plasma current), density effects when injecting into a near vacuum, the gap widths, and low- $Z$  impurities using an improved radiation model. Simulations are planned to be extended to the NSTX Upgrade<sup>5</sup> and other tokamaks and to include the transition to auxiliary current drive, e.g., by neutral beams.

## ACKNOWLEDGMENTS

We thank W. H. Meyer for computational support at LLNL. S. M. Kaye's detailed comments on the manuscript greatly improved its clarity. This work was performed under the auspices of the U.S. Department of Energy by Lawrence Livermore National Laboratory under Contract DE-AC52-07NA27344, by the PSI Center (University of Wisconsin) under Grant DE-FC02-05ER54813, by the University of Washington under Grant DE-FG02-99ER54519 AM08, by the University of New Hampshire under Grant DE-FG02-12ER55115 and by Princeton Plasma Physics Laboratory under Contract DE-AC02-09CH11466. Some simulations used resources of the National Energy Research Scientific Computing Center, which was supported by the Office of

Science of the U.S. Department of Energy under Contract No. DE-AC02-05CH11231.

- <sup>1</sup>R. Raman, B. A. Nelson, M. G. Bell, S. Gerhardt, H. W. Kugel, B. LeBlanc, R. Maingi, and J. Menard, *Phys. Rev. Lett.* **97**, 175002 (2006).
- <sup>2</sup>R. Raman, T. R. Jarboe, D. Mueller, B. A. Nelson, M. G. Bell, M. Ono, T. Bigelow, R. Kaita, B. LeBlanc, R. Maqueda, J. Menard, S. Paul, L. Roquemore, and the NSTX Research Team, *Phys. Plasmas* **14**, 056106 (2007).
- <sup>3</sup>R. Raman, D. Mueller, T. R. Jarboe, B. A. Nelson, M. G. Bell, M. Ono, T. Bigelow, R. Kaita, B. LeBlanc, K. C. Lee, R. Maqueda, J. Menard, S. Paul, and L. Roquemore, *Nucl. Fusion* **47**, 792 (2007).
- <sup>4</sup>R. Raman, D. Mueller, B. A. Nelson, T. R. Jarboe, S. Gerhardt, H. W. Kugel, B. LeBlanc, R. Maingi, J. Menard, M. Ono, S. Paul, L. Roquemore, S. Sabbagh, V. Soukhanovskii, and NSTX Research Team, *Phys. Rev. Lett.* **104**, 095003 (2010).
- <sup>5</sup>R. Raman, D. Mueller, S. C. Jardin, T. R. Jarboe, B. A. Nelson, M. G. Bell, S. P. Gerhardt, E. B. Hooper, S. M. Kaye, C. E. Kessel, J. E. Menard, M. Ono, V. Soukhanovskii, and the NSTX Research Team, *Nucl. Fusion* **53**, 073017 (2013).
- <sup>6</sup>R. Raman, S. C. Jardin, J. Menard, T. R. Jarboe, M. Bell, D. Mueller, B. A. Nelson, and M. Ono, *Nucl. Fusion* **51**, 113018 (2011).
- <sup>7</sup>T. R. Jarboe, *Plasma Phys. Controlled Fusion* **36**, 945 (1994).
- <sup>8</sup>T. R. Jarboe, M. A. Bohnet, A. T. Mattick, B. A. Nelson, and D. J. Orvis, *Phys. Plasmas* **5**, 1807 (1998).
- <sup>9</sup>A. J. Redd, B. A. Nelson, T. R. Jarboe, P. Gu, R. Raman, R. J. Smith, and K. J. McCollam, *Phys. Plasmas* **9**, 2006 (2002).
- <sup>10</sup>R. Raman, T. R. Jarboe, B. A. Nelson, V. A. Izzo, R. G. O'Neill, A. J. Redd, and R. J. Smith, *Phys. Rev. Lett.* **90**, 075005 (2003).
- <sup>11</sup>M. Nagata, T. Kanki, N. Fukumoto, and T. Uyama, *Phys. Plasmas* **10**, 2932 (2003).
- <sup>12</sup>J. B. Taylor, *Phys. Rev. Lett.* **33**, 1139 (1974).
- <sup>13</sup>T. R. Jarboe, *Fusion Technol.* **15**, 7 (1989).
- <sup>14</sup>R. A. Bayliss, C. R. Sovinec, and A. J. Redd, *Phys. Plasmas* **18**, 094502 (2011).
- <sup>15</sup>C. R. Sovinec, A. H. Glasser, T. A. Gianakon, D. C. Barnes, R. A. Nebel, S. E. Kruger, D. D. Schnack, S. J. Plimpton, A. Tarditi, and M. S. Chu, *J. Comp. Phys.* **195**, 355–386 (2004).
- <sup>16</sup>A. J. Redd, T. R. Jarboe, B. A. Nelson, R. G. O'Neill, and R. J. Smith, *Phys. Plasmas* **14**, 112511 (2007).
- <sup>17</sup>F. Ebrahimi, E. B. Hooper, C. R. Sovinec, and R. Raman, *Phys. Plasmas* **20**, 090702 (2013).
- <sup>18</sup>E. B. Hooper, R. Raman, J. E. Menard, and C. R. Sovinec, *Bull. Am. Phys. Soc.* **55**(15), 44 (2010).
- <sup>19</sup>D. D. Ryutov, B. I. Cohen, R. H. Cohen, and E. B. Hooper, *Phys. Plasmas* **12**, 084504 (2005).
- <sup>20</sup>E. B. Hooper, B. I. Cohen, H. S. McLean, R. D. Wood, C. A. Romero-Talamás, and C. R. Sovinec, *Phys. Plasmas* **15**, 032502 (2008).
- <sup>21</sup>B. I. Cohen, C. A. Romero-Talamás, D. D. Ryutov, E. B. Hooper, L. L. LoDestro, H. S. McLean, T. L. Stewart, and R. D. Wood, *Phys. Plasmas* **16**, 042501 (2009).
- <sup>22</sup>E. B. Hooper, C. R. Sovinec, R. Raman, and J. E. Menard, *Bull. Am. Phys. Soc.* **56**(12), 255 (2011).